Energy Storage Materials 54 (2023) 570–578

Contents lists available at ScienceDirect

Energy Storage Materials

journal homepage: www.elsevier.com/locate/ensm

Scalable production of hydrogen evolution corrosion resistant Zn-Al alloy anode for electrolytic MnO_2/Zn batteries

Jifei Sun [a,b], Xinhua Zheng [a], Ke Li [a], Gang Ma [d], Ting Dai [e], Boyuan Ban [c], Yuan Yuan [a], Mingming Wang [a], Mingyan Chuai [a], Yan Xu [a,b], Zaichun Liu [a], Taoli Jiang [a], Zhengxin Zhu [a], Jian Chen [c,*], Hanlin Hu [b,*], Wei Chen [a,*]

[a] Department of Applied Chemistry, School of Chemistry and Materials Science, Hefei National Research Center for Physical Sciences at the Microscale, University of Science and Technology of China, Hefei, Anhui 230026, China
[b] Hoffmann Institute of Advanced Materials, Shenzhen Polytechnic, Shenzhen, Guangdong 518000, China
[c] Key Lab of Photovoltaic and Energy Conservation Materials, Institute of Solid State Physics, HFIPS, Chinese Academy of Sciences, Hefei 230031, China
[d] School of Materials Science and Engineering, China University of Petroleum (East China), Huangdao District, Qingdao, Shandong 266580, China
[e] School of Mechanical Engineering, Beijing Institute of Petrochemical Technology, Daxing District, Beijing 102617, China

ARTICLE INFO

Keywords:
Electrolytic MnO_2/Zn battery
Large-scale energy storage
Hydrogen evolution corrosion
Zn-Al alloy
Large-scale fabrication

ABSTRACT

Electrolytic MnO_2/Zn battery has attracted significant attention for large-scale energy storage due to its advantages of high energy density and low cost. However, the acidic electrolyte used to maintain the Mn^{2+}/MnO_2 chemistry causes severe and irreversible hydrogen evolution corrosion (HEC) on the Zn anode. Herein, we present a scalable, metallurgical Al alloying approach to mitigate the HEC of Zn and prolong the battery's cycle life. Through various *in situ* and *ex situ* characterizations, it is demonstrated that the HEC on Zn-Al alloy electrode is effectively inhibited in the acidic electrolyte with and without the electric field effect. The outstanding anti-HEC capability of the Zn-Al alloy anode enables the electrolytic MnO_2/Zn-Al battery with a high discharge voltage of more than 1.9 V at 1 C, a more stable cycle performance, and an enhanced cycle life comparing with the MnO_2/Zn battery. Meanwhile, the experimental and COMSOL simulation results also reveal that the preferential but with slow corrosion speed of Al matrix in Zn-Al alloy is the key factor to improve the anti-HEC capability. This work exhibits the practicality of alloying strategy to produce scalable and robust Zn alloy anodes for the electrolytic MnO_2/Zn battery in the large-scale energy storage field.

1. Introduction

With the fast development of temporally intermittent renewable energy, large-scale energy storage technologies have attracted great interest [1–3]. Currently, lithium-ion batteries (LIBs) dominate the power storage landscape due to their high energy density, but the key elements of Li/Co resource reserves, safety, and environmental friendliness for LIBs remain as concerns [4,5]. In contrast, rechargeable aqueous zinc ion batteries have been widely considered as one of the excellent candidates for large-scale energy storage due to their non-inflammability, high theoretical capacities (820 mAh g^{-1}), and abundant resource reserves [6–9]. Among various Zn ion batteries, aqueous MnO_2/Zn batteries are highly appealing due to their low cost, environmental benignity, and various valence states of manganese (Mn)-based oxides (Mn^{2+}, Mn^{3+}, Mn^{4+} and Mn^{7+}) [10]. However, traditional MnO_2/Zn batteries make use of only one electron redox process of Mn^{4+}/Mn^{3+} at the cathode, which limits their capacity to be 308 mAh g^{-1} and output voltages of 1.2–1.4 V vs. Zn^{2+}/Zn [11–13]. Recently, Cui and co-workers proposed a new Mn^{2+}/MnO_2 deposition/stripping chemistry with a two-electron-transfer redox reaction, which delivered a high capacity of 616 mAh g^{-1} and a high output voltage of ~1.23 V vs. SHE [14]. Based on this electrolytic Mn^{2+}/MnO_2 chemistry, aqueous electrolytic MnO_2/Zn batteries with a high theoretical discharge voltage of 1.99 V have been developed and attracted much research interest recently [15–20].

Although the electrolytic MnO_2/Zn battery exhibits an eye-catching electrochemical performance, it still faces some critical challenges, which impede its practical applications [21,22]. According to the working principles of the electrolytic MnO_2/Zn batteries [23], as shown in the Eqs. (1)–(3),

* Corresponding authors.
E-mail addresses: jchen@ipp.ac.cn (J. Chen), hanlinhu@szpt.edu.cn (H. Hu), weichen1@ustc.edu.cn (W. Chen).

https://doi.org/10.1016/j.ensm.2022.10.059
Received 20 October 2022; Accepted 29 October 2022
Available online 30 October 2022

Cathode: $MnO_2 + 4H^+ + 2e^- \leftrightarrow Mn^{2+} + 2H_2O\ E^0 = 1.23$ V (1)

Anode: $Zn^{2+} + 2e^- \leftrightarrow Zn\ E^0 = -0.76$ V (2)

Overall: $MnO_2 + 4H^+ + Zn \leftrightarrow Mn^{2+} + 2H_2O + Zn^{2+}\ \Delta E = 1.99$ V (3)

HEC: $Zn + 2H^+ \rightarrow Zn^{2+} + H_2\uparrow$ (4)

the redox reaction at the cathode indicates that an acidic electrolyte condition can facilitate the dissolution of MnO_2 during the discharge process and thus improve the reversibility of the Mn^{2+}/MnO_2 reaction [24]. However, the acidic electrolyte is prone to trigger drastic irreversible HEC of Zn anode (Eq. (4)) [25], and enhances the activity of the competing reactions of H^+/H_2 during the Zn plating process [26,27], which deteriorates the cycle life of battery. Besides, those side reactions can in turn decrease the proton content in the electrolyte, which is harmful to the reversibility of the Mn^{2+}/MnO_2 reaction. These correlated issues ultimately result in the degradation of electrochemical performance particularly the cycle life of the electrolytic MnO_2/Zn battery.

To address the hydrogen evolution induced problems in the electrolytic MnO_2/Zn battery, many efforts have been devoted to the electrolyte [28–30], cell structure design [16,17,31], and separator [32]. Liu et al. used a weak acid of CH_3COOH to replace the strong acid of H_2SO_4 to reduce the proton concentration in the electrolyte and to mitigate the HEC of Zn [28]. However, the decrease of proton concentration deteriorates the reversibility of the Mn^{2+}/MnO_2 reaction. Moreover, the Zn still suffers HEC in the electrolyte with the CH_3COOH additive. Hu et al. designed a new battery structure to differ the pH of catholyte and anolyte by ion exchange membranes [31]. Although the improved electrochemical performances have been achieved, protons can still pass through the ion exchange membrane, leading to the decrease of pH of the anolyte. Yuan et al. fabricated PVA-based proton-barrier membrane to decouple acidic catholyte with mild anolyte [32]. The discontinuous hydrogen bond network can effectively obstruct proton migration to inhibit HEC of Zn. Nevertheless, the protons still pass through the proton barrier membrane and trigger the HEC of Zn over the long-term cycle test. Hence, it is highly desirable to fabricate an anti-HEC anode for the applications of the electrolytic MnO_2/Zn batteries.

Alloy materials have been widely used in batteries owing to their unique properties, such as fast ion diffusion kinetics [33,34], good air-stability [35], and anti-corrosion [36]. In the Zn-ion battery field, Zn alloys were used to inhibit dendrite growth in the mild acidic electrolytes [37–39], and mitigate the corrosion in the alkaline electrolyte [40,41]. Inspired by those progress, we screen out suitable alloying elements according to the electrolyte condition, and exhibit a Zn-Al alloy synthesized by a facile and scalable metallurgic approach to replace Zn as the anode material for the electrolytic MnO_2/Zn batteries in this study. Comparing with metallic Zn electrode, the preferential but with slow corrosion speed of Al matrix in Zn-Al alloy protects the Zn matrix from the acid corrosion, and thus enhances the anti-HEC capability of Zn-Al alloy in the acidic electrolyte. Beneficial from the anti-HEC advantages of the Zn-Al alloy, the Zn-Al alloy electrode shows a longer lifespan and higher hydrogen evolution overpotential in the acidic electrolyte. The electrolytic MnO_2/Zn battery constructed with the Zn-Al alloy anode also presents much superior long-term cycling stability. Besides, the facile preparation process of Zn-Al alloy can be mass-produced for the practical large-scale energy storage applications.

2. Results and discussion

2.1. Design principles of Zn alloys as anodes

Some primary principles for Zn-based alloys have been applied to the design of Zn anodes for the electrolytic MnO_2/Zn batteries. One is that the standard redox potential of alloying elements should be lower than that of Zn, because alloying elements with high standard potentials will introduce micro-galvanic cells and accelerate the corrosion of the Zn matrix. The second principle is that the metals of alloying elements should have low costs for practical application, ideally lower than Zn (Zn: ~3600 USD per ton). Hence, considering these two principles, Al (-1.66 V vs. SHE, ~2600 USD per ton), Mn (-1.18 V vs. SHE, ~2200 USD per ton), and Mg (-2.37 V vs. SHE, ~3700 USD per ton) were screened out that can be potential candidates for the fabrication of Zn alloy materials. The third principle is that the metals of alloying elements should have lower corrosion rates in the acidic solutions than that of Zn. To compare their anti-HEC capability, the four pure metal foils, i.e., Al, Mn, Mg, and Zn, were immersed in the acidic solution with 0.075 M H_2SO_4 additive. As shown in Fig. S1, many small bubbles emerged on the Zn metal surface, implying that the HEC occurred on the Zn. As for metallic Mn and Mg foils, severe bubbles appeared on their surfaces, indicating that they have worse corrosion resistance than that of Zn foil in the acidic solution. However, almost no bubbles were observed on the surface of Al foil even after a prolonged immersion time, demonstrating that metallic Al has an excellent corrosion resistant property in the acidic conditions. Hence, Al was chosen as the alloying element for the preparation of Zn alloy in this study.

2.2. Preparation and characterization of Zn-Al alloys

According to the phase diagram of Zn-Al system [42], the Zn-Al alloy is composed of Zn and Al matrixes without intermetallic compound. We applied a directional solidification approach to fabricate Zn-Al alloy, which can improve the purity of Zn and Al matrixes, and avoid the formation of micro-galvanic cells to improve the corrosion resistance. The directional solidification process was proceeded by gradually moving the molten metals out of the heating zone along one direction and then solidifying them (Fig. 1a: Step 1). This technique was widely used in the fields of purification [43,44] and single crystal growth [45], suggesting the capability of scalable synthesis of the Zn-Al alloy by this industrial mature method. According to the direction solidification technical characteristics, a eutectic Zn-Al alloy (88% Zn and 12% Al in atomic ratio) was chosen to obtain an even distribution of Zn and Al matrixes in the Zn-Al alloy. Through a four-step preparation process, viz. melting and directional solidification, slicing, rolling, and annealing (Figs. 1a and S2), ~100 μm thick Zn-Al alloy and Zn electrodes were synthesized (Fig. S3). The optical metallographs of the synthesized Zn-Al alloy and Zn are shown in Fig. 1b and 1c. Distinguished from the metallographic structure of Zn with polygonal grains, the Zn-Al alloy exhibits a typical eutectic structure with ordered alternating Zn and Al lamellae. The XRD results show that the major peaks in the Zn-Al alloy (red line) and the Zn foil (black line) correspond to the Zn phase (JCPDS 04-0831), and the weak peaks presented in the Zn-Al alloy (the magnified images in Fig. 1d) are attributed to the Al phase (JCPDS 04-0787) (Fig. 1d). The SEM and EDS characterizations of the Zn-Al alloy further demonstrate a uniform distribution of the alternating Zn and Al lamellae (Fig. 1e). The average inter-lamellar spacing (the thickness of Zn lamellae) of the synthesized Zn-Al alloy is ~0.94 μm, and the detailed distribution of inter-lamellar spacing of the Zn-Al alloy is shown in Fig. S4. In addition, a eutectic Zn-Al alloy with a larger inter-lamellar spacing (Zn-Al-LS) was synthesized by increasing the pulling speed during the directional solidification process. As shown in Fig. S5, the metallographic picture indicates that the Zn-Al-LS alloy also has a typical eutectic structure with ordered alternating Zn and Al lamellae. The average inter-lamellar spacing of Zn-Al-LS is ~1.3 μm, and the detailed distribution of inter-lamellar spacing of Zn-Al-LS is shown in Fig. S6.

2.3. HEC resistance performance of Zn-Al alloy

Before evaluating the HEC resistance performance of Zn-Al alloy electrode, the occurring reactions of Zn-Al alloy during the charging and

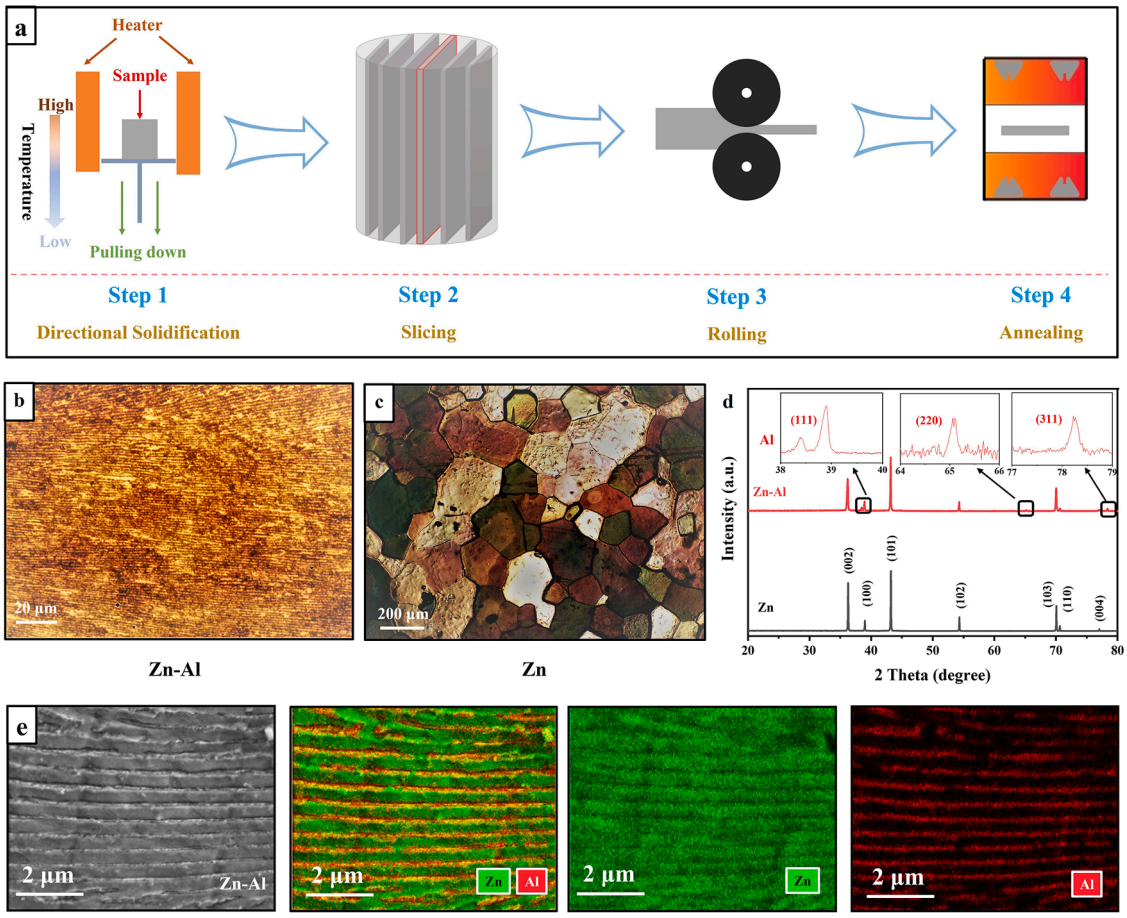

Fig. 1. (a) Schematic diagram of the preparation process of Zn-Al alloy. Optical metallographs of (b) Zn-Al alloy and (c) metallic Zn after etching with Keller reagent for 60 s. (d) XRD patterns of metallic Zn and Zn-Al alloys (the inset XRD patterns show the Al peaks of Zn-Al alloy). (e) SEM image and EDS elemental mapping of the eutectic phase of Zn-Al alloy.

discharging process were firstly studied by a three-electrode system, where Zn-Al alloy foils were used as working electrode and counter electrode simultaneously, and a mercurous sulfate electrode was used as reference electrode. A cyclic voltammogram (CV) test was implemented in the acidic electrolyte (1 M $ZnSO_4$ - 0.075 M H_2SO_4 – 0.1 M NaCl). Comparing with Zn||Zn symmetrical cell, the CV curve of Zn-Al||Zn-Al symmetrical cell exhibits almost the same plating/stripping transition potential (Fig. 2a), which indicates that the reactions (Zn plating/stripping) occurring on Zn-Al alloy electrode are the same as those of metallic Zn electrode during the charging and discharging process. In addition, the competing reaction of H^+/H_2 on Zn and Zn-Al alloy electrodes was evaluated by linear sweep voltammetry (LSV) test in the acidic solution (0.075 M H_2SO_4 – 0.1 M NaCl). As shown in Fig. 2b, the overpotential of hydrogen evolution on the Zn-Al alloy electrode is 93 mV larger than that of the Zn electrode at the current density of 10 mA cm^{-2}, indicating that the activity of the competing reaction of H^+/H_2 on anode is suppressed by using the Zn-Al alloy electrode, benefiting to improving the efficiency of Zn deposition. The aim of removing $ZnSO_4$ from the electrolyte for the LSV test is to eliminate the influence of overlapping Zn deposition and H_2 evolution.

As for HEC resistance performance of Zn-Al alloy electrode, various characterizations were used to compare the differences between Zn-Al alloy electrode and metallic Zn electrode in the conditions with and without the electric field effect. In the presence of the electric field, the linear polarization measurements were implemented to analyze the HEC resistance performance of the Zn-Al alloy and Zn by LSV in the 0.075 M H_2SO_4 - 0.1 M NaCl solution. As shown in Fig. 2c, the fitted corrosion current of Zn-Al alloy is 1.197 mA cm^{-2}, which is less than one third of metallic Zn (4.173 mA cm^{-2}), indicating better HEC resistance of the Zn-Al alloy electrode in the acidic electrolyte. In addition to the LSV test, *in-situ* detection of the H_2 production on Zn and Zn-Al alloy during cycling was also implemented by gas chromatography. The *in-situ* detection device is shown in Fig. S7, and the results are shown in Fig. 2d. The Zn-Al alloy electrode delivers about one-fourth of H_2 production rate of metallic Zn electrode, demonstrating excellent anti-HCE capability of the former during the cycling. Furthermore, the cycle performances of Zn-Al||Zn-Al and Zn||Zn symmetrical cells were evaluated. The symmetrical cell was assembled in a beaker configuration with excessive acidic electrolyte (0.075 M H_2SO_4 - 0.1 M NaCl - 1 M $ZnSO_4$, i.e., the electrodes can be completely corroded.), and the size of the electrodes immersing in the electrolyte is 1 cm * 1 cm. As shown in Fig. 2e, the voltage of Zn||Zn cell started to increase gradually around 1900 min due to the severe corrosion of Zn electrode. As the cycle progresses, the voltage increases suddenly around 2500 min, which suggests that the metallic Zn electrodes are corroded completely, and no contact exists between the metallic Zn electrode and the electrolyte (inset of Fig. 2e). In contrast, the Zn-Al alloy electrodes remain intact whereas the Zn||Zn symmetrical cell failed completely. The Zn-Al||Zn-Al symmetrical cell delivers a stable voltage profile for more than 8000 min, which is ~4 times longer than that of the Zn||Zn symmetrical cell. In addition, the cycle performance of Zn-Al-LS|| Zn-Al-LS symmetrical cell also delivers 3000–3500 min lifetime in the same test conditon (Fig. S8), which is still longer than that of Zn, but is shorter than that of Zn-Al alloy with smaller inter-lamellar spacing. The reasons for the decrease of cycling life of Zn-Al-LS||Zn-Al-LS symmetrical cell will be analyzed later. Besides, the cycle performance of symmetrical cells was further evaluated with a

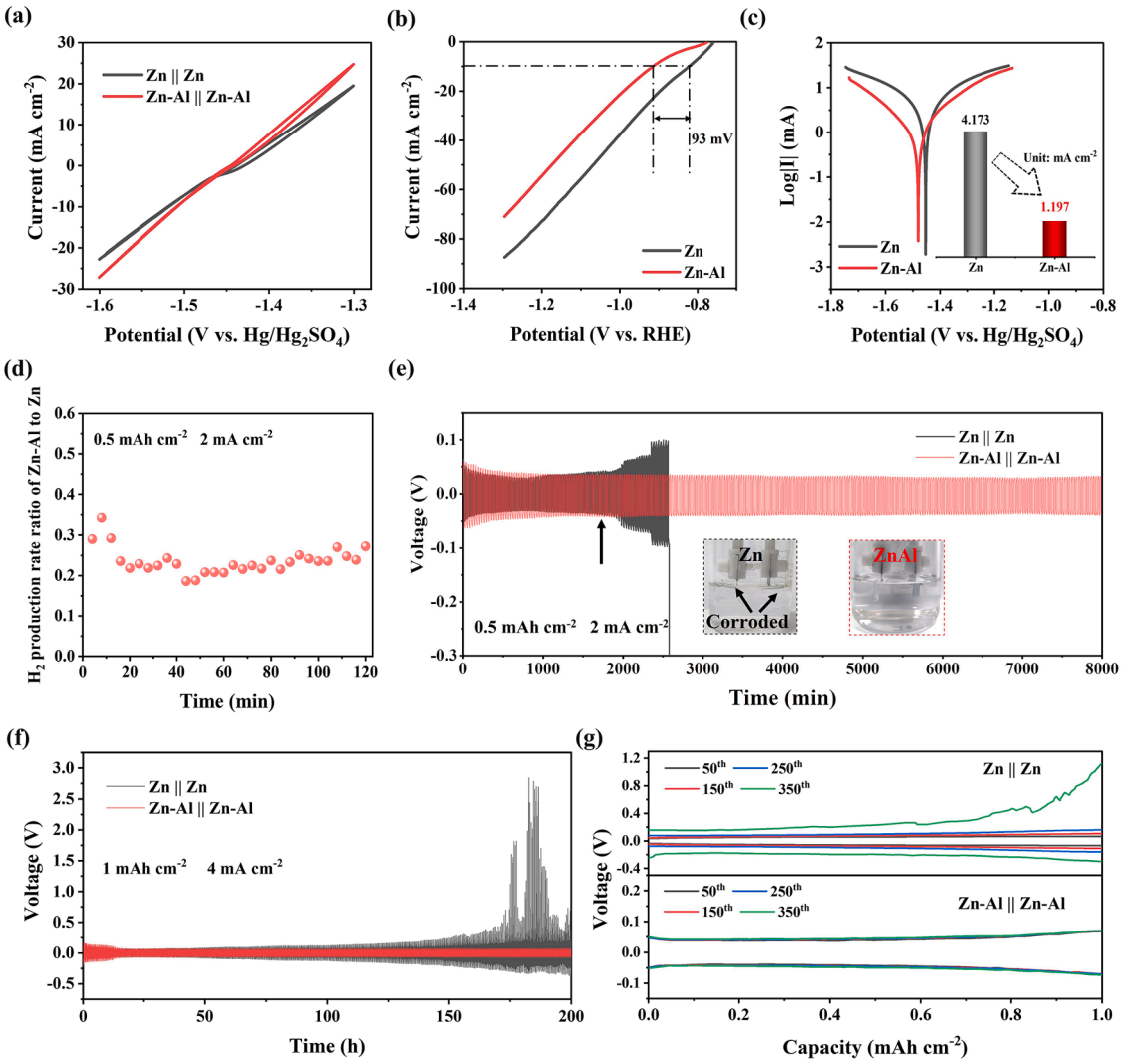

Fig. 2. HEC resistance performance of Zn and Zn-Al alloy electrodes. (a) Cyclic voltammogram of the Zn||Zn and Zn-Al||Zn-Al symmetrical cells. (b) HER properties of metallic Zn and Zn-Al alloy electrodes in the acidic electrolyte. (c) Linear polarization curves of the Zn and Zn-Al alloy electrodes in the acidic electrolyte. (d) *In-situ* detection of H_2 production rate ratio of Zn-Al alloy electrode to the metallic Zn electrode during cycling in the acidic electrolyte. (e) Cycling performance of symmetrical cells of Zn||Zn and Zn-Al||Zn-Al in the beaker cells with excessive acidic electrolyte at 2 mA cm^{-2} with the capacity of 0.5 mAh cm^{-2} (the inset photos show the morphology of Zn||Zn and Zn-Al||Zn-Al beaker cells after cycling). (f) Cycling performance of Zn||Zn and Zn-Al||Zn-Al symmetrical cells assembled in the pouch cells with limited acidic electrolyte. (g) Voltage profiles of Zn||Zn and Zn-Al||Zn-Al symmetrical cells assembled in the pouch cells.

larger areal capacity. As shown in Fig. S9, the cycle life of Zn-Al||Zn-Al symmetrical cell is still longer than that of Zn||Zn cell. Apart from the cycle tests in the beaker cell with excessive acidic electrolyte, the symmetrical cells were also assembled in the pouch cells with limited acidic electrolyte (i.e., the electrodes cannot be corroded completely.) (Fig. S10). Benefiting from the excellent anti-HEC capability of Zn-Al alloy electrode, the Zn-Al||Zn-Al cell delivers a stable cycle performance, while the Zn||Zn cell shows a huge polarization after cycling for 175 h, as shown in Fig. 2f and 2g. The reason for the huge polarization of Zn||Zn symmetrical cell may be ascribed to the severe corrosion around the electrode lug, leading to poor electrical contact, as shown in Fig. S11.

As for the HEC resistance performance of Zn-Al alloy electrode in the absence of the electric field effect, the immersion test was implemented in the acidic electrolyte (0.075 M H_2SO_4 - 0.1 M NaCl - 1 M $ZnSO_4$). The *in-situ* detection of the H_2 production of Zn and the Zn-Al alloy soaking in the acidic electrolyte was carried out by gas chromatography (GC). As shown in Fig. 3a, the Zn-Al alloy electrode delivers about one-tenth of H_2 production rate of metallic Zn electrode, implying that the speed of HEC of Zn is ~10 times faster than that of the Zn-Al alloy in the acidic electrolyte under the resting condition. Apart from the GC test, the pH changes of the electrolyte and the morphology of Zn and Zn-Al alloy after immersing in the acidic electrolyte for 1020 min are shown in Fig. 3b. Obviously, the Zn-Al alloy retains an intact and dense morphology, while the metallic Zn exhibits severe corrosion. Furthermore, the pH changes of the electrolytes indicated by the pH papers also demonstrate the excellent anti-HEC capability of the Zn-Al alloy in the acidic environment without the electric field effect. To better understand the difference in intrinsic corrosion process of Zn and Zn-Al alloy electrodes, localized electrochemical impedance spectroscopy (LEIS) was used to analyze the HEC process of Zn and Zn-Al alloy from the microscopic point of view. The LEIS is considered as a semi-quantitative and visual testing technique, which is suitable to unveil the material's intrinsic corrosion behaviors [46]. The schematic of the testing device in a three-electrode system is shown in Fig. 3c, where Ag/AgCl, Pt and Zn/Zn-Al alloy were used as reference electrode, counter electrode, and working electrode, respectively. An acidic electrolyte composed of 0.075 M H_2SO_4 - 0.1 M NaCl was used for the LEIS tests to eliminate the influence of overlapping Zn deposition and H_2 evolution. As shown in Fig. 3d and 3e, the impedance of the Zn-Al alloy is about an order of

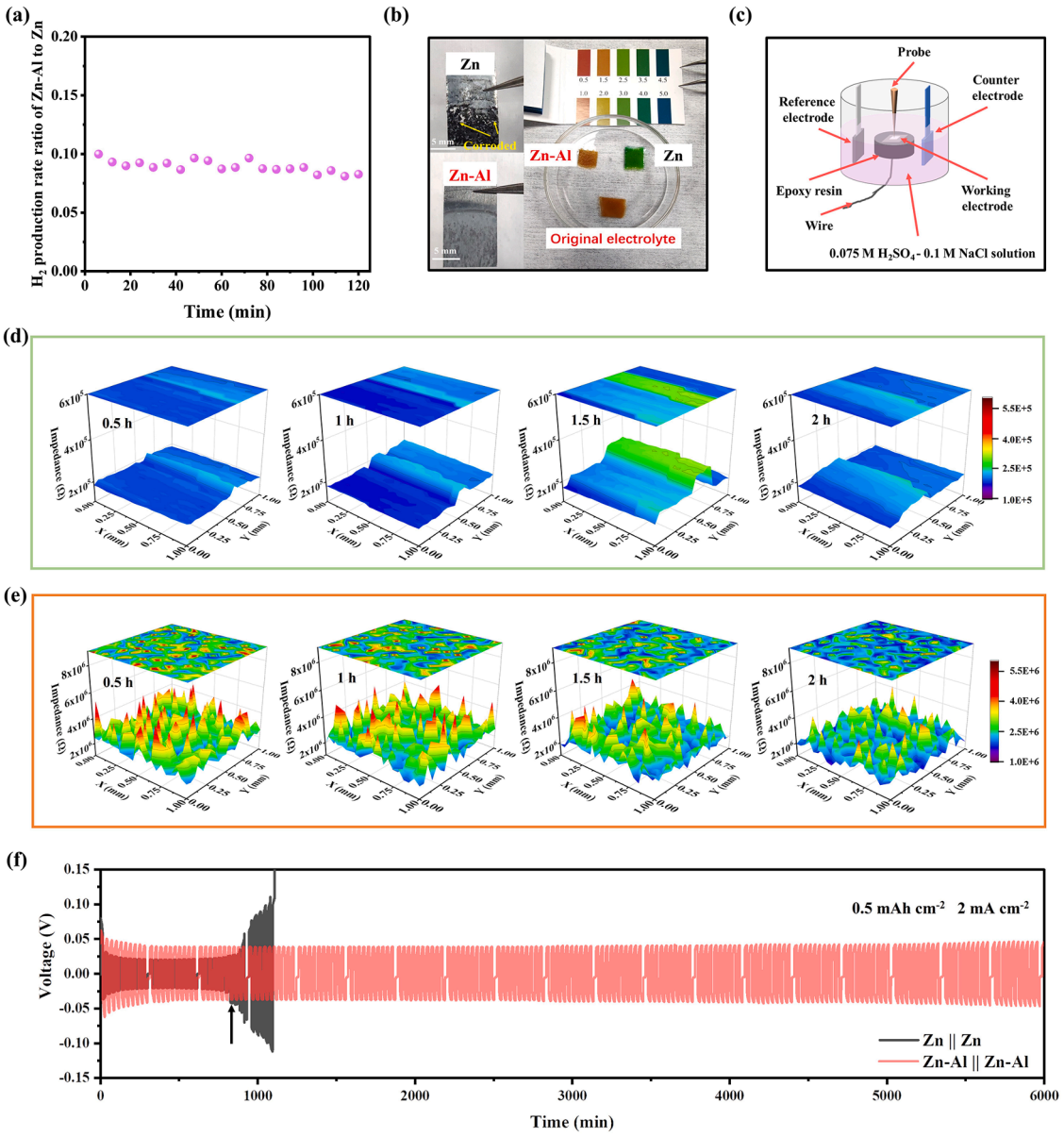

Fig. 3. (a) *In-situ* detection of H_2 production rate ratio of Zn-Al alloy to Zn in the acidic electrolyte without the electric field effect. (b) Photos of the corroded Zn and Zn-Al alloy foils and the pH changes of electrolytes after immersing in the acidic electrolyte for 1020 min. (c) Schematic of the LEIS testing device with a three-electrode system. Localized electrochemical impedance spectroscopy tests: (d) Change of LEIS mapping of metallic Zn electrode with the immersing time increased from 0.5 h to 2 h; (e) Change of LEIS mapping of Zn-Al alloy electrode with the immersing time increased from 0.5 h to 2 h. (f) Dynamic measurements of Zn||Zn and Zn-Al||Zn-Al symmetrical cells with a combination of Zn stripping/plating cycling at intervals of 15 min.

magnitude higher than that of Zn, which suggests a low reactivity of the Zn-Al alloy with protons, and the results are also consistent with the GC tests. In terms of the different corrosion behaviors, Zn electrode exhibits a relatively uniform impedance distribution, suggesting that the corrosion speed is almost the same in the entire testing area (Fig. 3d). Meanwhile, the impedance distribution of Zn remains almost unchanged with the increase of immersion time. Notably, a high impedance area appeared first and then disappeared with the immersion time increased from 1.5 h to 2 h, which may be attributed to the formation of an oxide layer on the surface of Zn and then the etching of the oxide layer [46, 47]. As for the Zn-Al alloy (Fig. 3e), the LEIS maps show violent fluctuations of the impedance distribution, possibly due to the distribution of Al and Zn matrixes. The different corrosion resistance of Zn and Al matrixes in the acidic solution causes the local impedance fluctuation. Different from the unchanged impedance distribution of the Zn electrode, the impedance of the Zn-Al alloy decreases with the immersion time, which may be attributed to the continued consumption of Al matrix in the Zn-Al alloy. Considering the HEC resistance performances of the Zn-Al alloy and Zn electrodes with and without the electric field effect, a dynamic measurement was performed in the beaker cell with excessive acidic electrolyte. A combination of electrochemical stripping/plating cycling (10 cycles, 2 mA cm^{-2}, 0.5 mAh cm^{-2}) at intervals of 15 min was implemented for the symmetrical cell test. As shown in Fig. 3f, the Zn||Zn symmetrical cell failed around ~800 min, while the Zn-Al||Zn-Al symmetrical cell exhibited ~ 6000 min stable cycles. The above tests demonstrate the excellent anti-HEC capability of the Zn-Al alloy electrode in the acidic electrolyte. Therefore, an improved electrochemical performance of the electrolytic MnO_2/Zn battery constructed with the Zn-Al alloy anode can be expected.

2.4. Electrochemical performance of MnO_2/Zn-Al full cell

The advantages of the Zn-Al alloy anode were further verified in a full cell. The electrolytic MnO_2/Zn full cell was assembled in a home-made electrolysis cell with limited Zn resources (~100 μm thick Zn/Zn-Al foils) and limited acidic electrolyte, as shown in Fig. S12. The cyclic voltammetry (CV) curves of the electrolytic MnO_2/Zn and MnO_2/Zn-Al batteries exhibit the similar shape with two pairs of redox peaks (Fig. 4a). The oxidation peak that starts from 1.9 V to 2.2 V vs. Zn^{2+}/Zn is ascribed to the deposition of MnO_2 and the reduction peak at ~1.8 V vs. Zn^{2+}/Zn is attributed to the dissolution of MnO_2 into Mn^{2+} ions. The enhanced charge and discharge currents of the MnO_2/Zn-Al battery suggest that the Zn-Al alloy is more conducive to the Zn plating/stripping than the Zn [37]. The EIS results further verify that the kinetics of Zn plating/stripping is improved by using Zn-Al alloy as the anode material. As shown in Fig. 4b, the charge transfer resistance of the MnO_2/Zn-Al battery (3.56 Ω) is lower than that of the MnO_2/Zn battery (12.35 Ω). Fig. 4c and 4d show the voltage curves of the MnO_2/Zn and MnO_2/Zn-Al batteries at various discharge rates. The battery was charged at a constant voltage of 2.2 V, and the morphology of the deposited MnO_2 is shown in Fig. S13. The SEM images and EDS mapping show that the MnO_2 is evenly deposited on carbon felt after the charging process. The electrodeposited MnO_2 was further identified by XRD characterization as Akhtenskite phase (JCPDS 30–0820) (Fig. S13c). In terms of discharge, both batteries show a flat discharge plateau of higher than 1.9 V at 1 C and higher than 1.7 V at 5 C. Moreover, the average discharge voltages at different rates of the MnO_2/Zn-Al battery are higher than that of the MnO_2/Zn battery (Fig. S14a). Benefiting from the higher discharge voltage of the MnO_2/Zn-Al battery, it delivers a higher energy efficiency than that of the MnO_2/Zn battery at various discharge rates, as displayed in Fig. S14b. After 70 cycles of rate test (~40 h), the macro- and the micro- morphology of the cycled metallic Zn and Zn-Al are shown in Fig. 4e and 4f. The macro-morphology of cycled Zn displays many corroded holes (Fig. 4e-1), indicating the severe HEC on the Zn anode during the test. Comparing with pristine Zn (Fig. 4e-2), the SEM images of the cycled Zn anode show step-like morphology (Fig. 4e-3/4), which is attributed to the anisotropy of the Zn metal. In contrast, no visible corroded holes appear on the cycled Zn-Al alloy (Fig. 4f-1), demonstrating good corrosion resistance of the Zn-Al alloy anode in electrolytic MnO_2/Zn battery. Meanwhile, the micro morphologies of the cycled Zn-Al anode (Fig. 4f-4) are obviously different from that of the cycled Zn anode. Comparing with pristine Zn-Al alloy anode (Fig. 4f-2), the corrosion pits on the surface of the cycled Zn-Al anode indicate that local corrosion occurred on the substrate. The EDS mapping images of the pristine Zn-Al alloy (Fig. 4f-3) and cycled Zn-Al alloy (Fig. 4f-4) indicate that Al matrix on the surface of Zn-Al alloy disappeared, which suggests that the Al matrix preferentially reacts with the protons. Notably, the difference between Fig. 1e and 4f-2 is ascribed

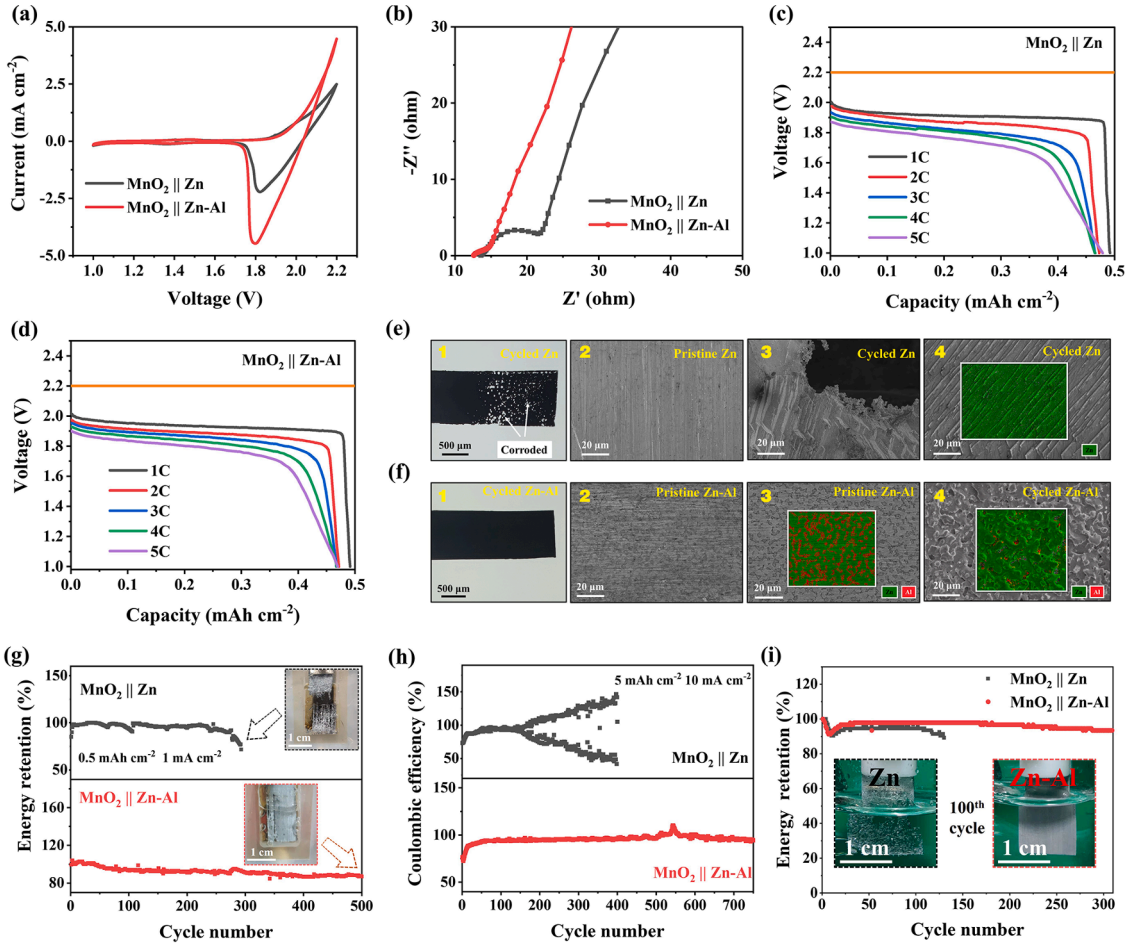

Fig. 4. Electrochemical performance of the electrolytic MnO_2/Zn-Al full cells. (a) Cyclic voltammogram of the electrolytic MnO_2/Zn and MnO_2/Zn-Al batteries. (b) EIS of the electrolytic MnO_2/Zn and MnO_2/Zn-Al batteries. Voltage profiles of (c) the electrolytic MnO_2/Zn and (d) the electrolytic MnO_2/Zn-Al batteries at various rates. Morphology changes of (e) the metallic Zn and (f) the Zn-Al alloy electrodes before and after 70 cycles. Energy retention of the electrolytic MnO_2/Zn and MnO_2/Zn-Al batteries for long-term cycles at different conditions: (g) in home-made cell with limited Zn resource and acidic electrolyte (the inset photos show the morphology of the cycled Zn and cycled Zn-Al alloy electrodes); (h) in the beaker cell with excessive Zn resource and limited acidic electrolyte; (i) in the H cell with limited Zn resource and excessive acidic electrolyte (the inset photos show the morphology of the cycled Zn and cycled Zn-Al alloy electrodes after 100 cycle).

to the Keller reagent alternative etching.

To examine the durability of the Zn-Al alloy anode in the full cells, long cycle tests were carried out at different conditions, and the results are shown in Fig. 4g and 4h. The long cycle tests were firstly implemented in the home-made electrolysis cell with limited Zn resource and acidic electrolyte. As shown in Fig. 4g, the Zn anode was severely corroded after ~300 cycle, while the Zn-Al alloy anode kept intact even after 500 cycles. Benefiting from the anti-HEC capability of the Zn-Al alloy electrode, the electrolytic MnO_2/Zn-Al battery delivers 86.98% energy retentions after 500 cycles. Besides, the MnO_2/Zn-Al battery also delivers a stable cyclability of over 1000 cycles, along with an average Coulombic efficiency over 96% and an energy retention of 85% at 5 C, as shown in Fig. S15. Apart from cycling in the home-made cell, the long cycle test was also operated in the beaker cell with excessive Zn resource and limited acidic electrolyte (1 M $ZnSO_4$ – 1 M $MnSO_4$ – 0.1 M H_2SO_4), as shown in Fig. S16a. The electrolytic MnO_2/Zn battery started to deviate after ~150 cycles, swinging up and down around the initial discharge capacity, of which the trend became more obvious with cycling (Figs. 4h and S16b). The fluctuation phenomenon is due to the effects of HEC of Zn anode, and pH change caused by cathode reaction, which becames more obvious as the pH value of electrolyte increases [28]. Because of the poor anti-HEC capability of metallic Zn anode, the protons react with metallic Zn are consumed quickly, leading to the pH increase of electrolyte, and the more obvious fluctuation phenomenon. In contrast, the electrolytic MnO_2/Zn-Al battery presents superior cycling stability with a 93.5% energy retention after 750 cycles. The excellent anti-HEC capability of Zn-Al alloy can keep the electrolyte at a relatively low pH, which not only can avoid the fluctuation phenomenon, but also can promote the reversibility of Mn^{2+}/MnO_2 reaction. Besides, the full cell was further operated in an H-cell with limited Zn resource and excessive acidic electrolyte (i.e., the anode can be corroded completely, Fig. S17). As shown in Fig. 4i, the Zn anode was corroded severely after 100 cycles, whereas the morphology of the Zn-Al alloy anode kept intact. Due to the excellent corrosion resistance of the Zn-Al

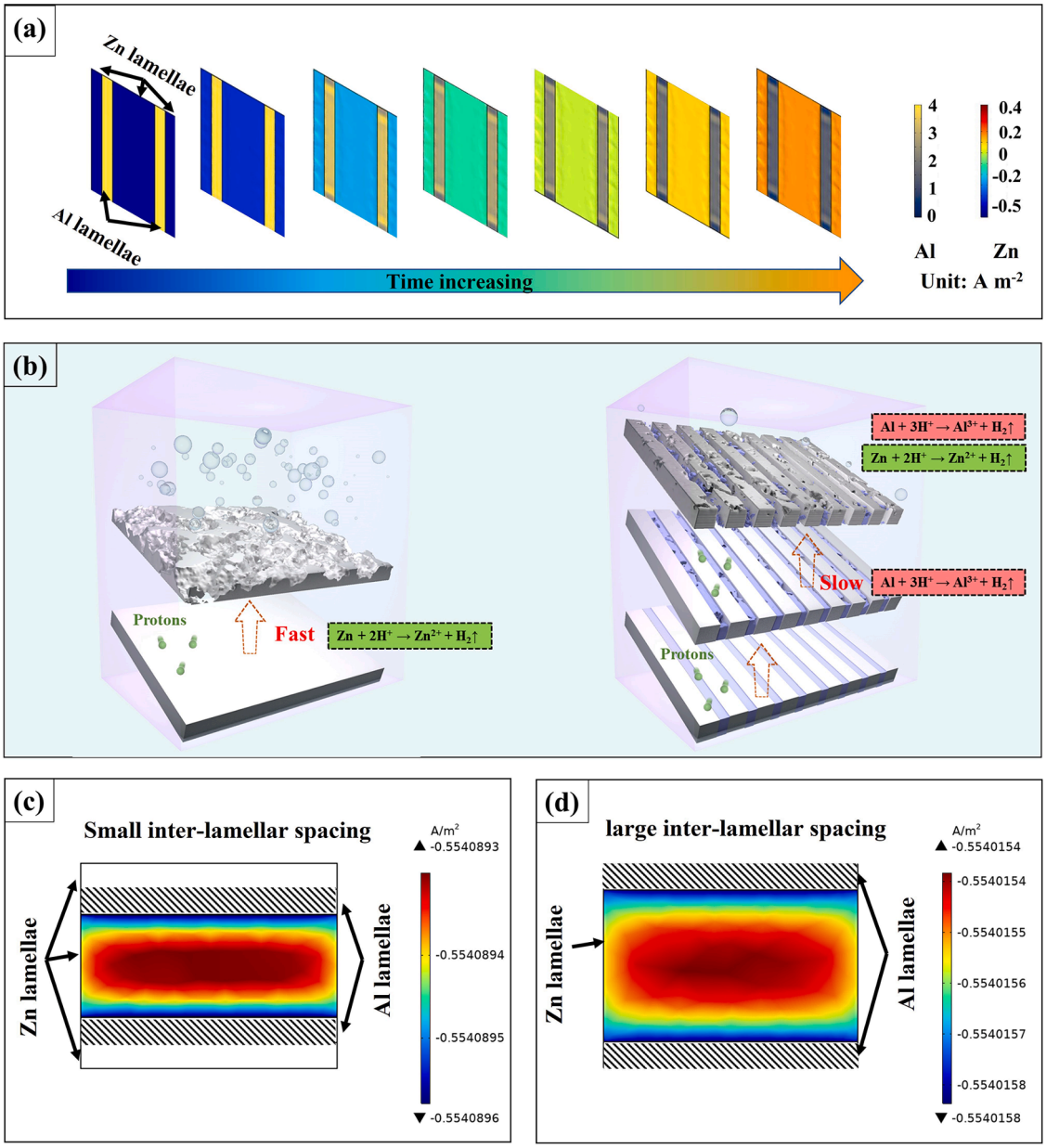

Fig. 5. The corrosion process simulation of Zn-Al alloy in the acidic electrolyte. (a) The changes of current density distribution on Zn and Al lamellae of Zn-Al alloy with time. (b) Schematic diagram of corrosion process of Zn and Zn-Al alloy electrodes. The local current density distribution on Zn lamellae of Zn-Al alloy with (c) small and (d) large inter-lamellar spacing at the initial stage.

alloy, the cycle life of the MnO_2/Zn-Al battery was increased to over 300 cycles with 93.4% energy retention, showing obvious advantages by replacing Zn with the Zn-Al alloy as the anode materials for the electrolytic MnO_2/Zn battery. Apart from the MnO_2 based battery, the Zn-Al alloy also displayed a better electrochemical performance in a corrosive Br_2/Zn full battery due to the superior corrosion resistance capability, as shown in Fig. S18.

2.5. COMSOL simulation

To understand the corrosion process and nature of the attenuation mechanism of the anti-HEC capability of the Zn-Al alloy, a finite-element method was used in COMSOL to model the corrosion process by simulating the current density distribution. The 3D models of Zn-Al alloy were constructed and shown in Fig. S19. The simulation results (Fig. 5a) indicate that the current polarities of Al and Zn matrices are positive and negative, respectively at the initial stage, which indicates that only the Al matrix shows the reactivity with protons, and the Zn matrix is protected by the external electrons provided by the Al matrix. With the time increase, however, the current density of Al matrix decreases, and the current polarity of Zn matrix gradually changes from negative to positive, suggest that Zn starts to show reactivity with protons. The decrease of the current density of the Al matrix is attributed to the consumption of Al, which in turn cause the decrease of the number of external electrons for Zn matrix protection, leading to the change of current polarity of Zn that has gradually enhanced its reactivity with protons. Consequently, it can be concluded that the introduction of preferential but slow corrosion speed of Al matrix into metallic Zn mitigates the HEC reaction in the acidic electrolyte, as the schematic diagram shown in Fig. 5b.

In addition, the simulated current density distribution of the Zn matrix in the Zn-Al alloy with different inter-lamellar spacing is shown in Fig. 5c and 5d. The difference of the scale values between Zn-Al and Zn-Al-LS alloys indicate that the intensity of protection current density of Zn matrix decreases with the increase of inter-lamellar spacing. Meanwhile, the area with low protection current density increases with the inter-lamellar spacing, which suggests an increase of the active area reacting with protons, leading to a faster corrosion rate. In addition, the weakened anti-HEC capability of Zn-Al-LS may be also attributed to the aggravated non-equilibrium solidification caused by the fast pulling-rate in the sample preparation process. The non-equilibrium solidification leads to a difficulty in the diffusion of Zn and Al atoms, which brings about a decrease of the purity of Zn and Al matrixes in the Zn-Al alloy that weakens the anti-HEC capability.

3. Conclusion

In summary, we applied a scalable directional solidification strategy to prepare Zn-Al alloys with tunable lamellar spacing to replace Zn anode, which showed excellent anti-hydrogen evolution corrosion property for the electrolytic MnO_2/Zn battery with much improved electrochemical performance. Various characterizations demonstrated that the Zn-Al alloy has a better corrosion resistance than that of Zn in the acidic electrolyte. The COMSOL simulation revealed that the Al matrix preferentially reacts with protons and provides electrons to protect Zn from corrosion. The excellent anti-HEC capability of the Zn-Al alloy anode enables the electrolytic MnO_2/Zn-Al battery with a more stable and longer cycle life than that of MnO_2/Zn battery in the different battery structures. Overall, this work provides a promising Zn alloying strategy to fabricate robust Zn-based anodes in large-scale production for Zn batteries, which can be extended to other metal-based energy storage devices.

Declaration of Competing Interest

The authors declare no competing financial interest.

Data Availability

Data will be made available on request.

Acknowledgments

The work was supported financially by the USTC (Grant No. KY2060000150), the Scientific Research Startup Fund for Shenzhen High-Caliber Personnel of Shenzhen Polytechnic (Nos. 6022310038k and 6022310049k), and National Natural Science Foundation of China (No. 51874272). The authors are thankful for the support from USTC Center for Micro and Nanoscale Research and Fabrication.

Supplementary materials

Supplementary material associated with this article can be found, in the online version, at doi:10.1016/j.ensm.2022.10.059.

Reference

[1] M. Pasta, C.D. Wessells, R.A. Huggins, Y. Cui, A high-rate and long cycle life aqueous electrolyte battery for grid-scale energy storage, Nat. Commun. 3 (1) (2012) 1149.
[2] A. Castillo, D.F. Gayme, Grid-scale energy storage applications in renewable energy integration: a survey, Energy Convers. Manag. 87 (2014) 885–894.
[3] T.M. Gür, Review of electrical energy storage technologies, materials and systems: challenges and prospects for large scale grid storage, Energy Environ. Sci. 11 (10) (2018) 2696–2767.
[4] C. Xie, Y. Li, Q. Wang, D. Sun, Y. Tang, H. Wang, Issues and solutions toward zinc anode in aqueous zinc ion batteries: a mini review, Carbon Energy 2 (4) (2020) 540–560.
[5] N. Zhu, K. Zhang, F. Wu, Y. Bai, C. Wu, Ionic liquid-based electrolytes for aluminum/magnesium/sodium ion batteries, Energy Mater. Adv. 2021 (2021) 1–29.
[6] X. Zheng, T. Ahmad, W. Chen, Challenges and strategies on Zn electrodeposition for stable Zn-ion batteries, Energy Storage Mater. 39 (2021) 365–394.
[7] L. Hong, L.Y. Wang, Y. Wang, X. Wu, W. Huang, Y. Zhou, K.X. Wang, J.S. Chen, Toward Hydrogen Free and Dendrite Free Aqueous Zinc Batteries: Formation of Zincophilic Protective Layer on Zn Anodes, Adv. Sci. 9 (6) (2022), 2104866.
[8] Z. Yi, G. Chen, F. Hou, L. Wang, J. Liang, Strategies for the stabilization of Zn metal anodes for Zn ion batteries, Adv. Energy Mater. 11 (1) (2020), 2003065.
[9] L.E. Blanc, D. Kundu, L.F. Nazar, Scientific challenges for the implementation of Zn Ion batteries, Joule 4 (4) (2020) 771–799.
[10] Y. Guo, Y. Zhang, H. Lu, Manganese based materials as cathode for rechargeable aqueous zinc ion batteries, Battery Energy 1 (2) (2022), 20210014.
[11] D. Wang, L. Wang, G. Liang, H. Li, Z. Liu, Z. Tang, J. Liang, C. Zhi, A superior delta-MnO_2 cathode and a self-healing Zn-delta-MnO_2 battery, ACS Nano 13 (9) (2019) 10643–10652.
[12] Y. Zeng, X. Zhang, Y. Meng, M. Yu, J. Yi, Y. Wu, X. Lu, Y. Tong, Achieving ultrahigh energy density and long durability in a flexible rechargeable quasi-solid-state Zn-MnO_2 battery, Adv. Mater. 29 (26) (2017), 1700274.
[13] Z. Liu, D. Wang, Z. Tang, G. Liang, Q. Yang, H. Li, L. Ma, F. Mo, C. Zhi, A mechanically durable and device-level tough Zn-Mno_2 battery with high flexibility, Energy Storage Mater. 23 (2019) 636–645.
[14] W. Chen, G. Li, A. Pei, Y. Li, L. Liao, H. Wang, J. Wan, Z. Liang, G. Chen, H. Zhang, J. Wang, Y. Cui, A Manganese–hydrogen battery with potential for grid-scale energy storage, Nat. Energy 3 (5) (2018) 428–435.
[15] D. Chao, W. Zhou, C. Ye, Q. Zhang, Y. Chen, L. Gu, K. Davey, S.Z. Qiao, An electrolytic Zn-MnO_2 battery for high-voltage and scalable energy storage, Angew. Chem. Int. Ed. 58 (23) (2019) 7823–7828.
[16] M. Li, Q. He, Z. Li, Q. Li, Y. Zhang, J. Meng, X. Liu, S. Li, B. Wu, L. Chen, Z. Liu, W. Luo, C. Han, L. Mai, A novel dendrite-free Mn^{2+}/Zn^{2+} hybrid battery with 2.3 V voltage window and 11000-cycle lifespan, Adv. Energy Mater. 9 (29) (2019), 1901469.
[17] G.G. Yadav, D. Turney, J. Huang, X. Wei, S. Banerjee, Breaking the 2 V barrier in aqueous zinc chemistry: creating 2.45 and 2.8 V MnO_2-Zn aqueous batteries, ACS Energy Lett. 4 (9) (2019) 2144–2146.
[18] M. Chuai, J. Yang, R. Tan, Z. Liu, Y. Yuan, Y. Xu, J. Sun, M. Wang, X. Zheng, N. Chen, W. Chen, Theory-driven design of cationic accelerator for high-performance electrolytic MnO_2-Zn batteries, Adv. Mater. 34 (33) (2022), e2203249.
[19] M. Wang, N. Chen, Z. Zhu, Y. Meng, C. Shen, X. Zheng, D. Liang, W. Chen, Electrode-less MnO_2-metal batteries with deposition and stripping chemistry, Small 17 (44) (2021), 2103921.
[20] M. Wang, N. Chen, Z. Zhu, Y. Meng, C. Shen, X. Zheng, D. Liang, W. Chen, Opportunities of aqueous manganese-based batteries with deposition and stripping chemistry, Adv. Energy Mater. 11 (5) (2020), 2002904.

[21] Z. Liu, L. Qin, B. Lu, X. Wu, S. Liang, J. Zhou, Issues and opportunities facing aqueous $Mn^{(2+)}/MnO_2$-based batteries, ChemSusChem 15 (10) (2022), 202200348.
[22] T. Zhang, Q. Chen, X. Li, J. Liu, W. Zhou, B. Wang, Z. Zhao, W. Li, D. Chao, D. Zhao, Redox mediator chemistry regulated aqueous batteries: insights into mechanisms and prospects, CCS Chem. 4 (9) (2022) 1–29.
[23] X. Zheng, Y. Wang, Y. Xu, T. Ahmad, Y. Yuan, J. Sun, R. Luo, M. Wang, M. Chuai, N. Chen, T. Jiang, S. Liu, W. Chen, Boosting electrolytic MnO_2-Zn batteries by a bromine mediator, Nano Lett. 21 (20) (2021) 8863–8871.
[24] G. Li, W. Chen, H. Zhang, Y. Gong, F. Shi, J. Wang, R. Zhang, G. Chen, Y. Jin, T. Wu, Z. Tang, Y. Cui, Membrane-free Zn/MnO_2 flow battery for large-scale energy storage, Adv. Energy Mater. 10 (9) (2020), 1902085.
[25] K. Wippermann, J.W. Schultze, R. Kessel, J. Penninger, The inhibition of zinc corrosion by bisaminotriazole and other triazole derivatives, Corros. Sci. 32 (2) (1991) 205–230.
[26] N. Adhoum, L. Monser, N. Bellakhal, J.E. Belgaied, Treatment of electroplating wastewater containing Cu^{2+}, Zn^{2+} and Cr(VI) by electrocoagulation, J. Hazard. Mater. 112 (3) (2004) 207–213.
[27.] C.M. Salles, G.C.G. de Oliveira, S.L. Díaz, O.E. Barcia, O.R. Mattos, Electrodeposition of Zn in acid sulphate solutions: pH effects, Electrochim. Acta 56 (23) (2011) 7931–7939.
[28] Z. Liu, Y. Yang, S. Liang, B. Lu, J. Zhou, pH-buffer contained electrolyte for self-adjusted cathode-free $Zn-MnO_2$ batteries with coexistence of dual mechanisms, Small Struct. 2 (11) (2021), 2100119.
[29] X. Zeng, J. Liu, J. Mao, J. Hao, Z. Wang, S. Zhou, C.D. Ling, Z. Guo, Toward a reversible Mn^{4+}/Mn^{2+} redox reaction and dendrite-free Zn anode in near-neutral aqueous Zn/MnO_2 batteries via salt anion chemistry, Adv. Energy Mater. 10 (32) (2020), 1904163.
[30] J. Lei, Y. Yao, Z. Wang, Y.C. Lu, Towards high-areal-capacity aqueous zinc-manganese batteries: promoting MnO_2 dissolution by redox mediators, Energy Environ. Sci. 14 (8) (2021) 4418–4426.
[31] C. Zhong, B. Liu, J. Ding, X. Liu, Y. Zhong, Y. Li, C. Sun, X. Han, Y. Deng, N. Zhao, W. Hu, Decoupling electrolytes towards stable and high-energy rechargeable aqueous zinc-manganese dioxide batteries, Nat. Energy 5 (6) (2020) 440–449.
[32] Y. Yuan, J. Yang, Z. Liu, R. Tan, M. Chuai, J. Sun, Y. Xu, X. Zheng, M. Wang, T. Ahmad, N. Chen, Z. Zhu, K. Li, W. Chen, A proton-barrier separator induced via hofmeister effect for high-performance electrolytic MnO_2-Zn batteries, Adv. Energy Mater. 12 (16) (2022), 2103705.
[33] H. Tian, Z. Li, G. Feng, Z. Yang, D. Fox, M. Wang, H. Zhou, L. Zhai, A. Kushima, Y. Du, Z. Feng, X. Shan, Y. Yang, Stable, high-performance, dendrite-free, seawater-based aqueous batteries, Nat. Commun. 12 (1) (2021) 237.
[34] M. Wan, S. Kang, L. Wang, H.W. Lee, G.W. Zheng, Y. Cui, Y. Sun, Mechanical rolling formation of interpenetrated lithium metal/lithium tin alloy foil for ultrahigh-rate battery anode, Nat. Commun. 11 (1) (2020) 829.
[35] J. Zhao, G. Zhou, K. Yan, J. Xie, Y. Li, L. Liao, Y. Jin, K. Liu, P.C. Hsu, J. Wang, H. M. Cheng, Y. Cui, Air-stable and freestanding lithium alloy/graphene foil as An alternative to lithium metal anodes, Nat. Nanotechnol. 12 (10) (2017) 993–999.
[36] W.R. Osório, L.C. Peixoto, A. Garcia, The effects of Ag content and dendrite spacing on the electrochemical behavior of Pb-Ag alloys for Pb-acid battery components, J. Power Sources 238 (2013) 324–335.
[37] S.B. Wang, Q. Ran, R.Q. Yao, H. Shi, Z. Wen, M. Zhao, X.Y. Lang, Q. Jiang, Lamella-nanostructured eutectic zinc-aluminum alloys as reversible and dendrite-free anodes for aqueous rechargeable batteries, Nat. Commun. 11 (1) (2020) 1634.
[38] Z. Qi, T. Xiong, T. Chen, C. Yu, M. Zhang, Y. Yang, Z. Deng, H. Xiao, W.S.V. Lee, J. Xue, Dendrite-free anodes enabled by a composite of a ZnAl alloy with a copper mesh for high-performing aqueous zinc-ion batteries, ACS Appl. Mater. Interfaces 13 (24) (2021) 28129–28139.
[39] J. Zheng, Z. Huang, Y. Zeng, W. Liu, B. Wei, Z. Qi, Z. Wang, C. Xia, H. Liang, Electrostatic shielding regulation of magnetron sputtered Al-based alloy protective coatings enables highly reversible zinc anodes, Nano Lett. 22 (3) (2022) 1017–1023.
[40] A.R. El-Sayed, H.S. Mohran, H.M. Abd El-Lateef, Effect of minor nickel alloying with zinc on the electrochemical and corrosion behavior of zinc in alkaline solution, J. Power Sources 195 (19) (2010) 6924–6936.
[41] E.M. Elrouby, H.A. El –Shafy Shilkamy, A. Elsayed, Development of the electrochemical performance of zinc via alloying with indium as anode for alkaline batteries application, J. Alloy. Compd. 854 (2021), 157285.
[42] Y.H. Zhu, H.C. Man, W.B. Lee, Exothermic reaction in eutectoid Zn-Al based alloys, Mater. Sci. Eng. A 268 (1-2) (1999) 147–153.
[43] J. Sun, Q. He, B. Ban, X. Bai, J. Li, J. Chen, Effect of Sn doping on improvement of minority carrier lifetime of Fe contaminated P-type multi-crystalline Si ingot, J. Cryst. Growth 458 (2017) 66–71.
[44] X. Bai, B. Ban, J. Li, Z. Fu, Z. Peng, C. Wang, J. Chen, Effect of Ti addition on b removal during silicon refining in Al-30%Si alloy directional solidification, Sep. Purif. Technol. 174 (2017) 345–351.
[45] X. Zhao, L. Liu, Z. Yu, W. Zhang, H. Fu, Microstructure development of different orientated nickel-base single crystal superalloy in directional solidification, Mater. Charact. 61 (1) (2010) 7–12.
[46] X. Zheng, Q. Liu, H. Ma, S. Das, Y. Gu, L. Zhang, Probing local corrosion performance of Sol-Gel/MAO composite coating on Mg Alloy, Surf. Coat. Technol. 347 (2018) 286–296.
[47] A.C. Bastos, M.G. Ferreira, A.M. Simões, Corrosion inhibition by chromate and phosphate extracts for iron substrates studied by EIS and SVET, Corros. Sci. 48 (6) (2006) 1500–1512.